Materials Advances

ROYAL SOCIETY OF CHEMISTRY

PAPER

View Article Online
View Journal | View Issue

Cite this: *Mater. Adv.*, 2023, 4, 4869

Impact of solvent-induced morphological changes on the hole transfer dynamics during a charge separation process†

Dongchan Lee,‡[a] Chang-Mok Oh,‡[b] Jiho Ryu,[a] Sung-Yeon Jang,[c] In-Wook Hwang *[b] and Shinuk Cho *[a]

Received 14th August 2023,
Accepted 11th September 2023

DOI: 10.1039/d3ma00546a

rsc.li/materials-advances

Despite a clear elucidation that the change in PM6:Y6 morphology with different solvents affects photovoltaic performance, the charge dynamics during the charge separation process resulting from these morphological changes have not been extensively studied. However, studies on mobility and photocurrent have shown that holes play a crucial role in charge generation and separation. In PM6:Y6 devices fabricated using chlorobenzene (PM6:Y6-CB), the reduced exciton dissociation probability is attributed to changes in hole transfer state due to morphological variations. In PM6:Y6 devices fabricated using chloroform (PM6:Y6-CF), the hole transfer state ($^{h}E_{CT}$) and Y6 highest occupied molecular orbital (HOMO) were almost degenerate. Consequently, the formation of lower effective $^{h}E_{CT}$, which can interfere with hole transfer, was minimized. Conversely, in PM6:Y6-CB, the overlapping region of $^{h}E_{CT}$ and Y6 HOMO shifts to the lower energy side, creating a significantly lower effective $^{h}E_{CT}$, which is energetically unfavorable for hole transfer. These findings from electroluminescence deconvolution analysis were validated using time-resolved photoinduced absorption spectroscopy. Consequently, the decrease in fill factor and current density in PM6:Y6-CB can be attributed to compromised hole transfer from Y6 HOMO to PM6 HOMO. This analysis underscores the importance of morphological changes in nonfullerene acceptor solar cells on hole transfer levels, ultimately affecting the charge separation efficiency.

Introduction

Organic photovoltaic cells (OPVs) based on a bulk heterojunction (BHJ) architecture of polymer donor and small molecular acceptor in the active layer have attracted significant attention owing to their significant potential in low-cost mobile energy sources.[1–4] Recent advances in the design and synthesis of narrow bandgap nonfullerene acceptors (NFAs) have led to power conversion efficiencies (PCEs) exceeding 18% in single-junction OPVs.[5–8] While the performance of OPVs depends mainly on the photoactive donor and acceptor materials, additional techniques, such as morphology control and interface engineering, play a crucial role in achieving maximum performance. Specifically, the morphology of the photoactive layer has a decisive impact on the performance of OPVs.[9–11]

Organic BHJ morphology is significantly affected by the processing solvent. It is not just a problem of solubility but also the interaction with the solvent molecule that affects the crystallinity of the donor and acceptor. Macroscopic morphology, such as the phase separation of donors and acceptors, can be effectively controlled by processing with solvent additives, such as 1-chloronaphthalene, 1,8-diiodooctane, and diphenyl ether, having selective solubility.[12–15] However, the main solvent is still important in forming the microscopic π–π stacking morphology within the phase. Solvent dependencies in performance are not exceptions to NFA-based OPVs (nf-OPV). This seems more serious in PM6:Y6, which is a high-performance nf-OPV.

In the fabrication of PM6:Y6 solar cells, chloroform (CF) is mainly used as a casting solvent for the photoactive layer. However, because of the low boiling point of CF, it poses difficulties when using various solution processes such as screen printing and doctor blade bar-coating. Interestingly,

[a] *Department of Physics and Energy Harvest Storage Research Center, University of Ulsan, Ulsan 44610, Republic of Korea. E-mail: sucho@ulsan.ac.kr*
[b] *Advanced Photonics Research Institute, Gwangju Institute of Science and Technology, Gwangju 61005, Republic of Korea. E-mail: hwangiw@gist.ac.kr*
[c] *Department of Energy Engineering, School of Energy and Chemical Engineering, Ulsan National Institute of Science and Technology (UNIST), Ulsan 44919, Republic of Korea*

† Electronic supplementary information (ESI) available: Device fabrication, characterizations, and details of Marcus theory and energy loss theory. See DOI: https://doi.org/10.1039/d3ma00546a

‡ These two authors (D. Lee and C.-M. Oh) contributed equally to this work.

PM6:Y6 solar cells made with a higher boiling point solvent such as chlorobenzene (CB) exhibited significantly lower performance than when using CF. This lower performance can be attributed to the unfavorable morphology of the photoactive layer.[16] PM6 has good solvent tolerance and can be processed using common solvents such as CB, CF, and toluene. Therefore, the morphology of PM6 is not greatly affected by the choice of solvent. In contrast, Y6 is somewhat sensitive to the processing solvent. Y6 forms a cube-like crystalline domain with a CB solvent. However, with CF solvent, Y6 formed a polymer-like crystalline domain *via* j-aggregation, which integrated into a unique two-dimensional (2D) transport network.[16] Thus, the higher performance of PM6:Y6 solar cells processed with CF could be due to the improved vertical charge transport caused by the polymer-like backbone channel tilted and extended in an out-of-plane direction from the substrate.

However, the fact that the change in mobility of electrons and holes was not as significant as the changes in morphology and efficiency (same order of magnitude around 10^{-4} for both CF and CB),[16] suggests that there may be other causes. The morphology changes in the photoactive layer may not only affect charge transport after charge separation but also affect the charge separation process. Although changes in charge transfer dynamics due to crystallinity have been highlighted by Zhu and coworkers,[16] the specific cause of the interruption of charge transfer has not been elucidated. Note that charge transfer dynamics are closely related to the charge transfer state between the PM6 donor and Y6 acceptor. On the other hand, further studies for the charge transfer state (CT state) of PM6:Y6 OPVs have shown that the contribution of the CT state to energy loss is quite small, resulting in high efficiency.[17–19] However, studies on the CT state of nf-OPVs (including PM6:Y6) have primarily focused on the electron-excited state. In nf-OPVs there are some differences in the charge transfer process compared to the solar cells based on a fullerene acceptor (f-OPV). In f-OPVs, excitons are mainly generated at the polymer donor, and electrons are transferred to the acceptor after separation at the interface of the donor and acceptor.[20–22] Thus, the electron transfer state ($^{e}E_{CT}$) that electrons pass through has a significant influence on device performance. However, in nf-OPVs, excitons are generated at the acceptor even more.[23–25] Therefore, the hole charge transfer state ($^{h}E_{CT}$) from the acceptor to the donor would influence the device performance more. Consequently, investigating the hole transfer state is a key factor in understanding the variation in charge transfer due to the morphology change.

In this study, we analyzed the effects of changes in BHJ morphology due to different solvents on charge dynamics related to charge separation. We confirmed the changes in the BHJ morphology and the resulting performance variation using two solvents: CB and CF. In addition, we analyzed the changes in the hole transfer state using EL deconvolution and time-resolved photoinduced absorption (PIA) spectroscopy. The decrease in exciton dissociation probability observed in the PM6:Y6 solar cell fabricated using CB (PM6:Y6-CB) was attributable to the change in hole transfer state due to morphological changes. For the PM6:Y6 solar cell fabricated using CF (PM6:Y6-CF), the density of state (DOS) of effective $^{h}E_{CT}$ was small, as the $^{h}E_{CT}$ and Y6 highest occupied molecular orbitals (HOMOs) were almost degenerate, and the lower $^{h}E_{CT}$, which can interfere with hole transfer, was also formed minimally. However, for PM6:Y6-CB, the overlapping region of $^{h}E_{CT}$ and Y6 HOMO shifted toward the lower energy side (upper $^{h}E_{CT}$), resulting in a significant formation of a lower effective $^{h}E_{CT}$ that served as a defect. These findings from EL deconvolution were also confirmed using TAS. Therefore, we concluded that the decrease in fill factor (FF) and current density (J_{sc}) in the PM6:Y6-CB was due to the deterioration of hole transfer from Y6 to PM6.

Results and discussion

Device characteristics

Fig. 1 shows the basic characterization results of the PM6:Y6 solar cells measured to confirm whether the performance differences between the devices fabricated using either CB or CF solvents were observed similarly compared with other literature reports.[26,27] Fig. 1a shows the chemical structure of the PM6 donor polymer and Y6 acceptor together with the device structure we utilized in this study. All devices were fabricated with the conventional structure using a PEDOT:PSS hole transport layer and Phen-NaDPO electron transport layer. Fig. 1b shows the J_{SC} *versus* applied voltage (V) characteristics of the devices fabricated using either CB or CF solvents. The PM6:Y6 solar cell fabricated using CF (PM6:Y6-CF) showed a PCE of 16.2% with a V_{OC} of 0.873 V, a J_{SC} of 25.5 mA cm^{-2}, and a FF of 0.725, while the device fabricated using CB (PM6:Y6-CB) showed a PCE of 12.2% with a V_{OC} of 0.817 V, a J_{SC} of 22.3 mA cm^{-2}, and a FF of 0.671 (see Table 1). The performance difference between PM6:Y6-CF and PM6:Y6-CB is also clearly identified in EQE measurements (Fig. 1c). All these results are consistent with the previous literature.[26,27]

As is known, these performance differences between PM6:Y6-CF and PM6:Y6-CB are clearly caused from morphology differences. Fig. S1 (ESI†) shows the morphology differences between PM6:Y6-CF and PM6:Y6-CB obtained by grazing-incident wide-angle X-ray scattering (GIWAXS). In the out-of-plane direction, both PM6:Y6-CF and PM6:Y6-CB showed a (010) diffraction peak (π–π stacking of PM6) in the same 2θ angle of $\sim$1.75 Å^{-1} (d-spacing of 3.59 Å). However, the peak intensity of the PM6:Y6-CB was clearly small compared to that of the PM6:Y6-CF. In the in-plane direction, the PM6:Y6-CF exhibited superior crystallinity of Y6 compared to that of the PM6:Y6-CB; in particular, the (020), (110), and (111) peaks showed well-ordered lamellar crystalline stacking. The GIWAXS results were well correlated with previous literature.[16] The atomic force spectroscopy (AFM) images of the morphology of PM6:Y6-CF and PM6:Y6-CB are presented in Fig. S2 (ESI†). The surface of the PM6:Y6-CF film showed uniform and well-ordered fibril structures with a root-mean-square (rms) roughness of 1.336 nm. In contrast, the PM6:Y6-CB film showed a

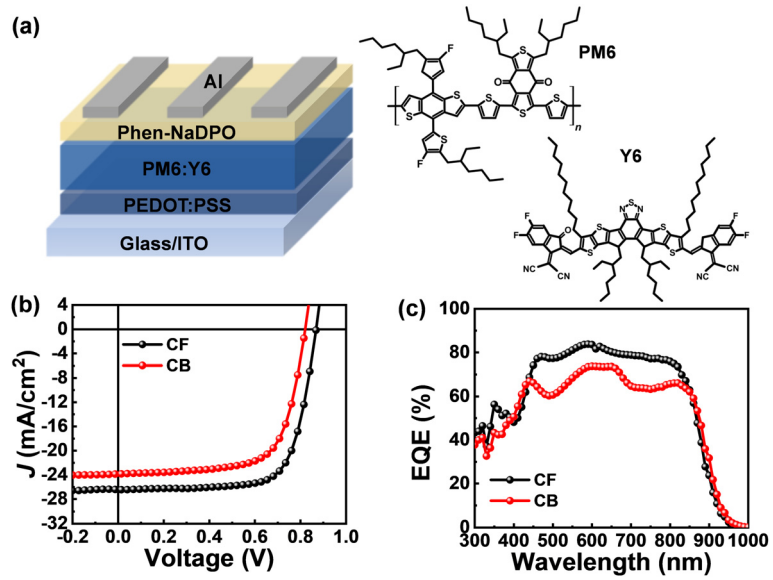

Fig. 1 (a) Device architecture and chemical structures of PM6 and Y6 used in this study. (b) *J V* curves and (c) external quantum efficiency spectra of PM6:Y6-CF and PM6:Y6-CB devices.

Table 1 Photovoltaic performances of solar cell devices used in this study

Solvent	J_{sc} (mA cm^{-2})	V_{oc} (V)	F.F. (%)	PCE[a] (%)
Chloroform	25.5 (25.35)	0.873 (0.865)	72.5 (71.1)	16.2 (15.6)
Chlorobenzene	22.3 (21.34)	0.817 (0.814)	67.1 (66.2)	12.2 (11.5)

[a] Values in parentheses were obtained by averaging 15 devices.

slightly aggregated morphology with a rms roughness of 2.415 nm.

Among the various factors that affect the performance of organic solar cells, it is expected that changes in charge carrier mobility will have the greatest impact due to these morphology differences. To investigate the difference in charge carrier mobility caused by morphology differences, a space-charge-limited current (SCLC) analysis was conducted on the PM6:Y6-CF and PM6:Y6-CB devices. Fig. 2 shows the SCLC measurements for the electron-only PM6:Y6-CF and PM6:Y6-CB devices (Fig. 2a) and the hole-only PM6:Y6-CF and PM6:Y6-CB devices (Fig. 2b). Hole mobility (μ_h) and electron mobility (μ_e) were calculated using the Mott-Gurney law,[28] and the hole trap density (n_t^h) and electron trap density (n_t^e) were determined through trap-filled limited voltage (V_{tfl}), which is the cross-point of the ohmic region and trap-filled-limit SCLC region. Details of device preparation and derivation of SCLC mobility and trap density are presented in the supplementary information. The calculated μ_h, μ_e, n_t^h and n_t^e are listed in Table 2. In our measurements, the μ_h was calculated to be relatively slower compared to μ_e in both PM6:Y6-CF and PM6:Y6-CB devices. In the PM6:Y6 system, it appears that the movement of electrons is faster overall than the movement of holes. In the comparison between PM6:Y6-CF and PM6:Y6-CB, there was not a significant difference in μ_e, while a large variation was observed in μ_h. Due to the significant difference in μ_h, the mobility balance between hole and electron was worse in PM6:Y6-CB compared to PM6:Y6-CF. However, this difference is not significant enough to explain the overall decrease in PCE. The relatively low μ_h was likely to be caused

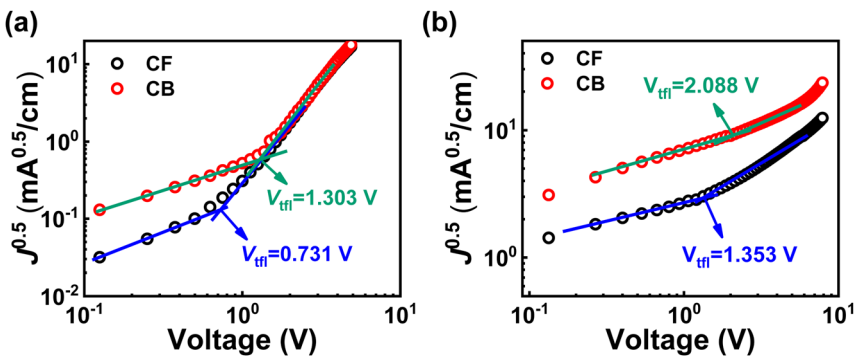

Fig. 2 $J^{1/2}$–V plots of (a) electron-only and (b) hole-only devices. Trap-filled limited voltage and trap density were obtained at the cross-point of the ohmic region and trap-filled-limited SCLC region.

Table 2 Electron, hole mobility, and trap density determined from SCLC measurements

Solvent	μ_e [cm^2 v^{-1} s^{-1}]	μ_h [cm^2 v^{-1} s^{-1}]	μ_h/μ_e	n_t^e [cm^{-3}]	n_t^h [cm^{-3}]
Chloroform	8.19×10^{-4}	1.76×10^{-4}	0.215	2.82×10^{16}	5.23×10^{16}
Chlorobenzene	7.39×10^{-4}	7.61×10^{-5}	0.103	5.04×10^{16}	8.08×10^{16}

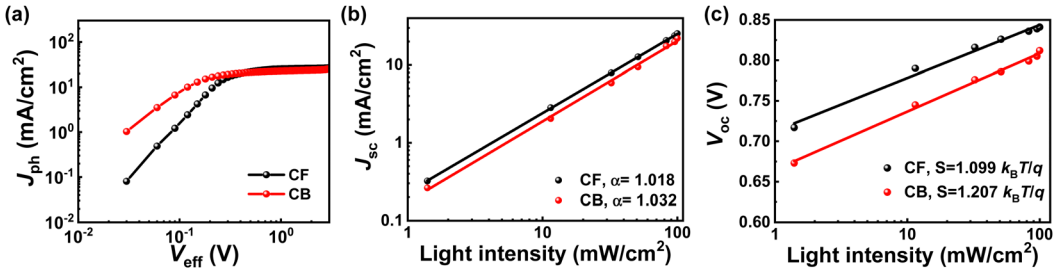

Fig. 3 (a) Photocurrent density (J_{ph}) *versus* effective voltage (V_{eff}) plots of PM6:Y6-CF and PM6:Y6-CB devices. G_{max} and $P(E,T)$ were calculated from the current density at the saturated region. (b) Light intensity-dependent J_{sc} and (c) V_{oc} of PM6:Y6-CF and PM6:Y6-CB devices.

by the high n_t^h. The n_t^h was observed to be higher in PM6:Y6-CB. One clear fact that can be inferred from the mobility analysis above is that the performance of PM6:Y6 solar cells is strongly correlated with hole transfer and transport dynamics.

To provide a deeper understanding of the impact of morphology changes induced by solvents on device parameters, we conducted a detailed device characterization analysis. Fig. 3a shows the relationship between photocurrent density (J_{ph}) and effective voltage (V_{eff}), which can be used to investigate the correlation between charge collection and exciton dissociation in the active layer. The maximum possible exciton generation rate (G_{max}) values were calculated using the equation $J_{sat} = qG_{max}L$,[29] where J_{sat} is the saturation photocurrent density, q is the electronic charge, and L is the active layer thickness. The exciton dissociation probability ($P(E,T)$) values were obtained from the ratio of J_{ph}/J_{sat}.[26] As shown in the results listed in Table 3, G_{max} for the PM6:Y6-CF was 1.61×10^{27} m^{-3} s^{-1} and G_{max} for the PM6:Y6-CB: was 1.47×10^{27} m^{-3} s^{-1}. The $P(E,T)$ of PM6:Y6-CF was 98.4% and the $P(E,T)$ of PM6:Y6-CB was 96.2%. The values of G_{max} and $P(E,T)$ both showed slightly improved values in the PM6:Y6-CF. Fig. 3b shows the relationship between Jsc and light intensity (I), which gives information about bimolecular recombination. In general, J_{sc} is proportional to I to the power of α.[30] Under short-circuit conditions, bimolecular recombination becomes negligible as α approaches 1.0 (weak bimolecular recombination). The fitted α values were 1.018 for PM6:Y6-CF and 1.032 for PM6:Y6-CB, both close to 1.0, indicating that both PM6:Y6-CF and PM6:Y6-CB were nearly free from bimolecular recombination loss. The charge recombination property near open-circuit conditions was evaluated by monitoring the device V_{OC} values with respect to I (Fig. 3c). The extracted ideality factor (k_BT/q) was 1.099 for PM6:Y6-CF. In the case of PM6:Y6-CB, a much larger ideality factor of 1.207 was observed, which indicates the enhanced trap-assisted recombination. In general, the difference in trap-assisted recombination is interpreted as a change in the first-order recombination that can occur during the charge separation process involving charge transfer (CT) states. Therefore, the results suggest that more first-order recombination associated with CT states occur at the PM6:Y6-CB. Overall, based on these results, it can be interpreted that the high efficiency in PM6:Y6-CF was not only due to the increase in charge transport characteristics through morphology improvement but also due to a fundamental increase in charge generation caused by dynamic changes in the charge separation process. On the other hand, in PM6:Y6-CB, some kind of change that caused energy loss was generated by the morphology change, which ultimately led to a decrease in the fundamental charge generation rate by affecting the charge separation process, resulting in a decrease in efficiency. In addition, according to mobility studies based on SCLC measurements, it can be inferred that holes are deeply involved in these charge generation and separation processes.

Table 3 Charge generation rate and dissociation probability from Fig. 3a

Solvent	G_{max} (m^{-3} s^{-1})	$P(E,T)$ (%)
Chloroform	1.61×10^{27}	98.4
Chlorobenzene	1.47×10^{27}	96.2

EL deconvolution & Hole CT state

To investigate the hole transfer dynamics, we have applied the idea of the EL deconvolution method to the PM6:Y6 solar cells fabricated using either CB or CF solvents. In the BHJ system based on fullerene acceptor (f-BHJ), all the charges that contribute to the onset part of the EQE are initially excited at the donor site, and then electrons are transferred to the acceptor through the electron transfer state ($^eE_{CT}$) (see Fig. S4a, ESI†). However, the onset part of the EQE of the PM6:Y6 blend is formed solely by the contribution of the Y6 acceptor itself (Fig. S4b and c in ESI†). Since the electron density excited in

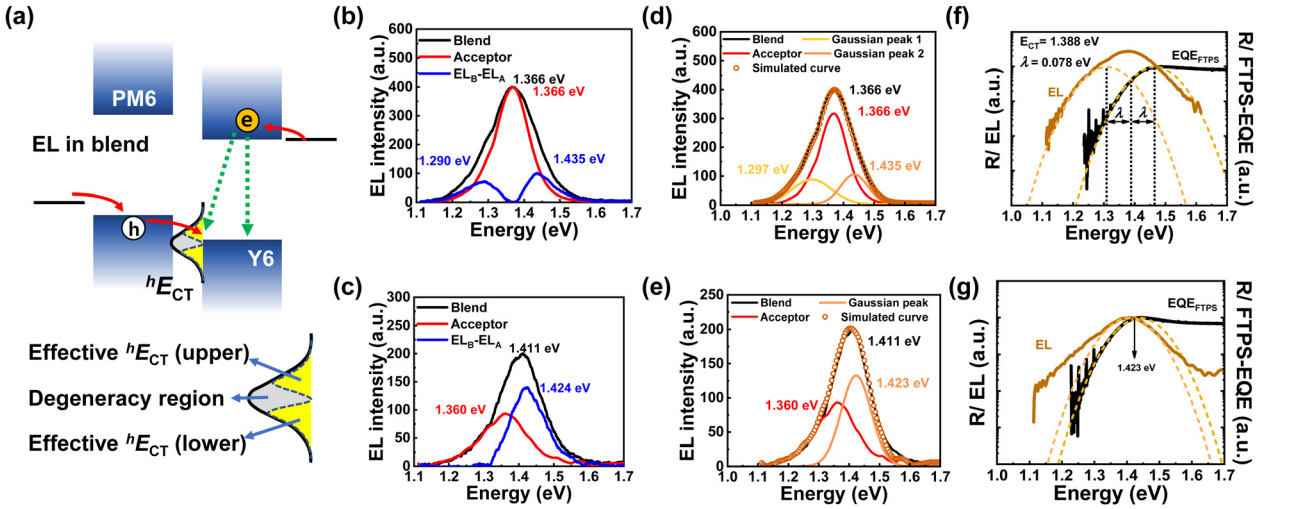

Fig. 4 (a) Schematic of the charge injection mechanism of the EL mode. The EL spectrum can be sorted into three parts: recombination with electrons at Y6's lowest unoccupied molecular orbital and (i) holes at Y6's HOMO (singlet transition), (ii) holes at the upper $^{h}E_{CT}$, and (iii) lower $^{h}E_{CT}$. (b), (c) EL_B, EL_A, and EL_B-EL_A spectra of CF-and CB-processed devices. (d) and (e) EL deconvolution using Gaussian fits based on the EL_B-EL_A spectrum. The simulated curve (orange circle) is obtained with the Gaussian peak of the $^{h}E_{CT}$ and EL_A spectrum.

the acceptor itself is already high, $^{e}E_{CT}$ located at the electron transfer pathway has little influence on the device performance. Rather, in the non-fullerene acceptor system, the hole transfer state ($^{h}E_{CT}$) occurring on the highest occupied molecular orbital (HOMO) side of the donor and acceptor is more important. In an EL measurement for the PM6:Y6 solar cells, electrons are injected directly into the acceptor's lowest unoccupied molecular orbital (LUMO) and holes are initially injected into the HOMO of the donor and then transferred to the acceptor through $^{h}E_{CT}$ (see Fig. 4a). Thus, the EL of the PM6:Y6 blend (EL_B) has constraints on both the singlet recombination of the acceptor and the radiative recombination *via* $^{h}E_{CT}$. Therefore, by deconvolution of EL_B, it is possible to extract out the $^{h}E_{CT}$ contribution.

Fig. 4b shows the difference between the EL_B and EL_A spectra obtained from PM6:Y6-CF. This difference in the EL spectrum (blue line) indicates the contribution of $^{h}E_{CT}$ to EL. Note that the PM6 donor polymer has minimal contribution (Fig. S4c, ESI†). To determine the exact peak position, Gaussian fits were performed on the EL_B, resulting in its spectrum being deconvoluted into three components. The peak in the center (1.372 eV) corresponds to the singlet radiative recombination between the acceptor's LUMO and HOMO. The peaks on both the low- and high-energy sides are caused by the effective $^{h}E_{CT}$ band. The $^{h}E_{CT}$ levels near the acceptor's HOMO are similar to a degenerate state, making them indistinguishable. Our focus lies in the energy range lower than the acceptor's HOMO (upper effective $^{h}E_{CT}$), which affects energy loss. The $^{h}E_{CT}$ levels within the energy region that is higher than the acceptor's HOMO (lower effective $^{h}E_{CT}$) contribute little to hole transfer and may play a role as a defect (or trap). On the contrary, in the PM6:Y6-CB solar cells, there is no difference between EL_B and EL_A in the low-energy region. The EL difference was observed only in higher energy regions (Fig. 4d and e). The Gaussian fit for the EL_B was deconvoluted into two components. The low-energy part of EL_B exactly overlaps with the EL_A. Thus, the effective $^{h}E_{CT}$ region is formed only on the lower side of the $^{h}E_{CT}$ band. The fact that the effective $^{h}E_{CT}$ is lower than the HOMO of the acceptor indicates yhe ingents. The low or site, insufficient hole transfer for charge separation. This charge separation problem is attributed to the low J_{sc} observed in PM6:Y6-CB.

Furthermore, evidence of more traps near the band edge in PM6:Y6-CB can be found in the absorption spectrum. In Fig. S3 (ESI†), the absorption of the Y6 region of the PM6:Y6-CF film shows a stiff onset, whereas the PM6:Y6-CB film shows a long-tail onset at around 1000 nm. This long-tailed onset is referred to as the Urbach tail, and the energy impact caused by the trap site can be calculated as the Urbach energy from the exponential fitting of the tail's exponential function:[31] $\alpha = \alpha_g \exp[E - E_g/E_u]$, where α is the absorption coefficient, α_g is the absorption coefficient at the bandgap, E is photon energy, E_g is bandgap, and E_U is Urbach energy. The Urbach energy of the PM6:Y6-CF film was 0.031 meV, and that of the PM6:Y6-CB film was 0.107 meV (Fig. S5, ESI†). From the above equation, the exponential slope is determined using the value of E_U, where a large value has a more tailed shape. As a result, the CB solvent leads to inferior crystallinity of Y6 and finally suppresses the V_{oc} due to more trap sites near the band edge.

Hole transfer properties

Based on the above results, the performance degradation in PM6:Y6-CB could be due to the suppression of hole transfer from PM6 to Y6 during the charge separation process. To gain a clearer understanding of the changes in the hole transfer characteristics during charge separation, which is caused by the variation in $^{h}E_{CT}$ due to morphological differences, we performed optical experiments using steady-state photoluminescence (PL) spectroscopy, time-correlated single photon counting (TCSPC), and transient absorption spectroscopy (TAS). Note that the electron transfer process was not

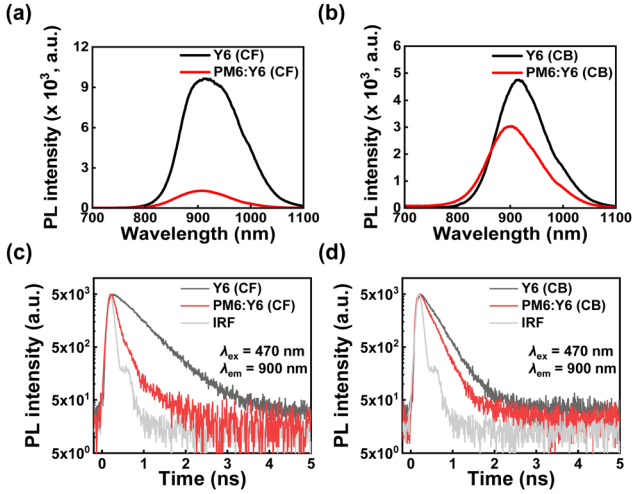

Fig. 5 Steady-state PL spectra of PM6:Y6 and Y6 films fabricated using (a) CF solvent and (b) CB solvent, and time-correlated single photon counting results for (c) CF solvent and (d) CB solvent.

Table 4 Exciton decay time and PL quenching efficiency (η_{PL}) from PL spectra. The exciton decay time is measured using time-correlated single photon counting measurements, and the PL quenching efficiency is calculated using the PL spectra of the PM6:Y6 blend and Y6 neat films

	Exciton decay time (ns)			
	τ_1	τ_2	τ_{avg}	η_{PL} (%)
PM6:Y6 (CF)	0.09 (98%)	0.53 (2%)	0.10	92.1
Y6 (CF)	0.52	—		
PM6:Y6 (CB)	0.12 (73%)	0.26 (27%)	0.16	31.8
Y6 (CB)	0.26	—		

considered because electrons from Y6 cannot be transferred to PM6 because of the large offset of LUMO of Y6 and LUMO of PM6. Therefore, residual PL intensity indicates an insufficient hole transfer process from Y6 to PM6. We obtained the PL spectra by dividing their absorption intensity at an excitation wavelength of 532 nm to compare the exciton separation yields. In comparison to the PM6:Y6-CB case, the Y6 PL intensity is more quenched by 92.1% in PM6:Y6-CF than in the PL quenching efficiency of PM6:Y6-CB by 31.8% (Fig. 5a and b). This enhanced PL quenching of Y6 in PM6:Y6-CF indicates a more efficient exciton separation, which is responsible for the improved J_{sc}. The exciton decay in the Y6 region at 900 nm becomes faster when transitioning from Y6 to PM6:Y6 (Fig. 5c and d) because of the hole transfer process from Y6 to PM6. Detailed fitted values were obtained by deconvolution fitting to a summation of exponential terms (see TCSPC measurements in supplementary information), and listed in Table 4. The fast and slow time constants in PM6:Y6-CF and PM6:Y6-CB can be attributed to hole transfer from Y6 to PM6 and exciton recombination in Y6, respectively. The hole transfer times of 0.09 ns for PM6:Y6-CF and 0.12 ns for PM6:Y6-CB were observed (Table 4). These results show enhanced charge separation in PM6:Y6-CF. However, note that the PL lifetime of the CF-processed pristine Y6 film (0.52 ns) was twice as long as that of the CB-processed pristine Y6 film (0.26 ns). These results were also observed in the blend film of PM6:Y6-CF and PM6:Y6-CB, and are consistent with steady-state PL spectra and the enhanced crystallinity of Y6 in CF, as obtained from GIWAX. In addition, we obtained the photoinduced absorption spectra and decay profiles of the PM6:Y6-CF and PM6:Y6-CB after photoexcitation at 650 nm using TAS (Fig. 6a and b). The initial 1 ps PIA band at ~1.347 eV corresponds to the singlet exciton state of Y6. After 1000 ps, a PIA band formed at ~1.292 eV, which was interpreted as $^{h}E_{CT}$. This precisely matches the position of the upper effective $^{h}E_{CT}$ analyzed through EL deconvolution (Fig. 4). However, in PM6:Y6-CB, the PIA band did not form at 1.292 eV but was maintained at a slightly higher energy side relative to the Y6 singlet state band. These results are also consistent with the EL deconvolution analysis. Fig. 6c shows the exciton decay profiles of PM6:Y6-CF and PM6:Y6-CB. The decay times and relative amplitudes were obtained by fitting them to a sum of exponential terms (Table 5). At 925 nm (1.34 eV, singlet state of Y6), PM6:Y6-CB shows two decay times of $\tau_1 = 110 \pm 9.5$ ps (54%) and >3000 ps (46%). The decay time of 110 ps is attributed to hole transfer from Y6 to PM6 based on the comparable fast time constant of 0.12 ns in the TCSPC result. The slow time constant of >3000 ps can be attributed to the characteristic of long-lived polarons. PM6:Y6-CF exhibited PIA decay time constants of 2.5 ± 0.5 ps (34%), 100.3 ± 10.4 ps (31%), and >3000 ps (35%). In contrast to PM6:Y6-CB, we observed a fast hole transfer time of 2.5 ps in PM6:Y6-CF. We characterized the average hole transfer time of 49.3 ± 5.1 ps based on weight averaging, considering the similarities with the increased PL quenching results. Therefore, fast hole

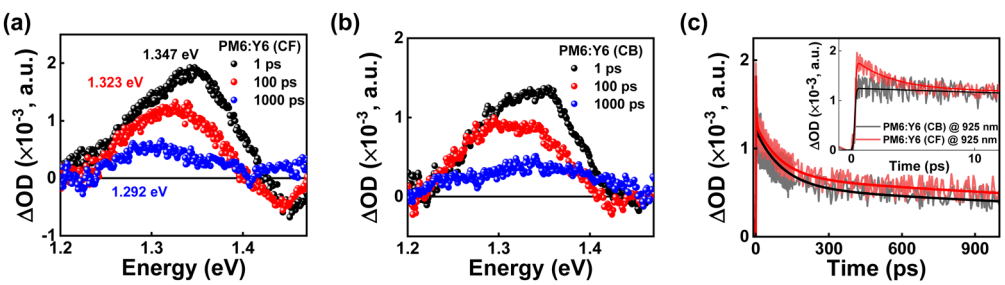

Fig. 6 Transient absorption spectra of (a) PM6:Y6-CF and (b) PM6:Y6-CB at the time of 1, 100, and 1000 ps. (c) Optical density decay profiles during 1000 ps at 925 nm (1.341 eV). Inset image is enlarged in the decaying region (~10 ps), indicating faster optical density decaying at the PM6:Y6-CF film.

Table 5 Exciton decay time obtained from TAS measurements

	Fitted decay times (ps)		
	τ_1	τ_2	τ_3
PM6:Y6 (CF)	2.5 ± 0.5 (34%)	100.3 ± 10.4 (31%)	>3000 (35%)
PM6:Y6 (CB)	110.2 ± 9.5 (54%)	>3000 (46%)	

transfer from Y6 to PM6 in PM6:Y6-CF reduced the charge recombination loss at the interface and enhanced the exciton separation yield within Y6, which contributed to improved J_{sc}.

Conclusions

In conclusion, the morphology that forms when different solvents are used for CB and CF appears to have an impact on the formation of the hole transfer level, which significantly affects the charge separation process. For PM6:Y6-CF, the $^{h}E_{CT}$ and Y6 HOMO were almost degenerate, indicating a smaller effective DOS of $^{h}E_{CT}$. This results in the formation of lower effective $^{h}E_{CT}$, which can interfere with hole transfer. In contrast, for PM6:Y6-CB, the overlapping area between $^{h}E_{CT}$ and Y6 HOMO shifts toward a lower energy (upper $^{h}E_{CT}$), resulting in a larger number of lower effective $^{h}E_{CT}$ that can act as deep trap levels (defects). The presence of $^{h}E_{CT}$ and its dependence on morphology was further confirmed using time-resolved PIA experiments. Furthermore, the increase in the defect level at the Urbach tail can be attributed to the influence of the lower effective $^{h}E_{CT}$ level. These morphological changes in NFA solar cells can affect the formation of the hole transfer level and charge separation efficiency. Therefore, for additional performance enhancement and high-performance NFA solar cell production, it is necessary to confirm the formation of the hole transfer level and its ease of transfer. This can be achieved using the simple EL deconvolution method used in this study.

Author contributions

D. Lee and C.-M. Oh contributed equally to this work.

Conflicts of interest

There are no conflicts to declare.

Acknowledgements

This work was supported by the National Research Foundation of Korea (2020R1A2C1003929, 2019R1A6A1A11053838, 2020M1A2A2080746) and by the GIST Research Institute (GRI) APRI grant funded by the GIST in 2022).

References

1 X. Zhang, Z. Lu, L. Ye, C. Zhan, J. Hou, S. Zhang, B. Jiang, Y. Zhao, J. Huang, S. Zhang, Y. Liu, Q. Shi, Y. Liu and J. Yao, *Adv. Mater.*, 2013, **25**, 5791–5797.
2 J. Yuan, Y. Zhang, L. Zhou, G. Zhang, H.-L. Yip, T.-K. Lau, X. Lu, C. Zhu, H. Peng, P. A. Johnson, M. Leclerc, Y. Cao, J. Ulanski, Y. Li and Y. Zou, *Joule*, 2019, **3**, 1140–1151.
3 L. Ma, S. Zhang, J. Zhu, J. Wang, J. Ren, J. Zhang and J. Hou, *Nat. Commun.*, 2021, **12**, 5093.
4 C. Zhu, J. Yuan, F. Cai, L. Meng, H. Zhang, H. Chen, J. Li, B. Qiu, H. Peng, S. Chen, Y. Hu, C. Yang, F. Gao, Y. Zou and Y. Li, *Energy Environ. Sci.*, 2020, **13**, 2459–2466.
5 L. Wang, C. Guo, X. Zhang, S. Cheng, D. Li, J. Cai, C. Chen, Y. Fu, J. Zhou, H. Qin, D. Liu and T. Wang, *Chem. Mater.*, 2021, **33**(22), 8854–8862.
6 L. Zhu, M. Zhang, J. Xu, C. Li, J. Yan, G. Zhou, W. Zhong, T. Hao, J. Song, X. Xue, Z. Zhou, R. Zeng, H. Zhu, C.-C. Chen, R. C. I. MacKenzie, Y. Zou, J. Nelson, Y. Zhang, Y. Sun and F. Liu, *Nat. Mater.*, 2022, **21**, 656–663.
7 J. Fu, P. W. K. Fong, H. Liu, C. Huang, X. Lu, S. Lu, M. Abdelsamie, T. Kodalle, C. M. Sutter-Fella, Y. Yang and G. Li, *Nat. Commun.*, 2023, **14**, 1760.
8 M. Deng, X. Xu, Y. Duan, L. Yu, R. Li and Q. Peng, *Adv. Mater.*, 2023, **35**, 2210760.
9 B. Jiang, Y. Wang, C. Liao, Y. Chang, Y. Su, R. Jeng and C. Chen, *ACS Appl. Mater. Interfaces*, 2021, **13**(1), 1076–1085.
10 J. S. Park, G. Kim, D. Lee, S. Lee, B. Ma, S. Cho and B. Kim, *Adv. Funct. Mater.*, 2020, **30**, 2005787.
11 K. Weng, L. Ye, L. Zhu, J. Xu, J. Zhou, X. Feng, G. Lu, S. Tan, F. Liu and Y. Sun, *Nat. Commun.*, 2020, **11**, 2855.
12 J. Lv, H. Tang, J. Huang, C. Yan, K. Liu, Q. Yang, D. Hu, R. Singh, J. Lee, S. Lu, G. Li and Z. Kan, *Energy Environ. Sci.*, 2021, **14**, 3044–3052.
13 Y. Ding, X. Zhang, H. Feng, X. Ke, L. Meng, Y. Sun, Z. Guo, Y. Cai, C. Jiao, X. Wan, C. Li, N. Zheng, Z. Xie and Y. Chen, *ACS Appl. Mater. Interfaces*, 2020, **12**(24), 27425–27432.
14 H. Choi, J. Lee, C. Oh, S. Jang, H. Kim, M. S. Jeong, S. H. Park and I. Hwang, *J. Mater. Chem. A*, 2019, **7**, 8805–8810.
15 Z. Zheng, E. He, J. Wang, Z. Qin, T. Niu, F. Guo, S. Gao, Z. Ma, L. Zhao, X. Lu, Q. Xue, Y. Cao, G. T. Mola and Y. Zhang, *J. Mater. Chem. A*, 2021, **9**, 26105–26112.
16 L. Zhu, M. Zhang, G. Zhou, T. Hao, J. Xu, J. Wang, C. Qiu, N. Prine, J. Ali, W. Feng, X. Gu, Z. Ma, Z. Tang, H. Zhu, L. Ying, Y. Zhang and F. Liu, *Adv. Energy Mater.*, 2020, **10**, 1904234.
17 L. Perdigón-Toro, L. Q. Phuong, S. Zeiske, K. Vandewal, A. Armin, S. Shoaee and D. Neher, *ACS Energy Lett.*, 2021, **6**(2), 557–564.
18 M. Pranav, T. Hultzsch, A. Musiienko, B. Sun, A. Shukla, F. Jaiser, S. Shoaee and D. Neher, *APL Mater.*, 2023, **11**(5), 061111.
19 Q. Guo, Q. Guo, Y. Geng, A. Tang, M. Zhang, M. Du, X. Sun and E. Zhou, *Mater. Chem. Front.*, 2021, **5**, 3257–3280.
20 K. Wang, C. Yi, C. Liu, X. Hu, S. Chuang and X. Gong, *Sci. Rep.*, 2015, **5**, 9265.
21 S. Li, W. Liu, C. Li, M. Shi and H. Chen, *Small*, 2017, **13**, 1701120.
22 M. Muntwiler, Q. Yang, W. A. Tisdale and X.-Y. Zhu, *Phys. Rev. Lett.*, 2008, **101**, 196403.

23 P. Chang, G. Li, X. Zhan and Y. Yang, *Nat. Photonics*, 2018, **18**, 131–142.
24 Y. Liu, L. Zuo, X. Shi, A. K.-Y. Jen and D. S. Ginger, *ACS Energy Lett.*, 2018, **3**(10), 2396–2403.
25 T. Wang, Z. Chen, J. Qiao, W. Qin, J. Liu, X. Wang, Y. Pu, H. Yin and X. Hao, *ACS Appl. Mater. Interfaces*, 2023, **15**(9), 12109–12118.
26 S. Bao, H. Yang, H. Fan, J. Zhang, Z. Wei, C. Cui and Y. Li, *Adv. Mater.*, 2021, **33**, 2105301.
27 B. Jiang, C. Chen, H. Liang, R. Jeng, W. Chien and Y. Yu, *Dyes Pigm.*, 2020, **181**, 108613.
28 W. E. I. Sha, X. Li and W. C. H. Choy, *Sci. Rep.*, 2014, **4**, 6236.
29 P. W. M. Blom, V. D. Mihailetchi, L. J. A. Koster and D. E. Markov, *Adv. Mater.*, 2007, **19**, 1551–1566.
30 L. J. A. Koster, M. Kemerink, M. M. Wienk, K. Maturová and R. A. J. Janssen, *Adv. Mater.*, 2011, **23**, 1670–1674.
31 F. Urbach, *Phys. Rev.*, 1953, **92**, 1324.